Colloids and Surfaces A: Physicochemical and Engineering Aspects 634 (2022) 127944

Contents lists available at ScienceDirect

Colloids and Surfaces A: Physicochemical and Engineering Aspects

journal homepage: www.elsevier.com/locate/colsurfa

Hybrid fibroin-nanocellulose composites for the consolidation of aged and historical silk

Chiara Cianci, David Chelazzi *, Giovanna Poggi, Francesco Modi, Rodorico Giorgi, Marco Laurati

Department of Chemistry "Ugo Schiff" and CSGI, University of Florence, Via della Lastruccia 3, 50019 Sesto Fiorentino, Florence, Italy

HIGHLIGHTS

- The restoration practice lack methods to remedy silk artifacts' degradation.
- We formulated tailored cellulose nanocrystals (CNC)-fibroin consolidants.
- CNC boosts the assembly of colloidal fibroin in compact structures at the nanoscale.
- CNC favors the formation of fibroin crystalline structures in hybrid films.
- Casting the CNC/fibroin films on degraded silk fully restored textile resistance.

GRAPHICAL ABSTRACT

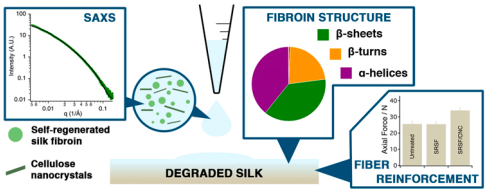

ARTICLE INFO

Keywords:
Self-regenerated silk fibroin
Cellulose nanocrystals
Hybrids
Composite materials
Silk restoration
Cultural Heritage conservation

ABSTRACT

Silk artifacts are a valuable artistic and historical heritage, but are prone to degradation that makes the fibers fragile, hindering the preservation of precious collections. Dispersions of self-regenerated silk fibroin (SRSF) can be used to cast films on aged fibers and recover their mechanical properties, but there appears to be a limit to the fibroin concentration in the dispersions, as too concentrated systems produce highly crystalline but mechanically brittle films. Alternatively, we propose here hybrid dispersions of SRSF and cellulose nanocrystals (CNC) with the aim to grant the aged fibers improved strength, taking advantage of the SRSF structuration induced by CNC, and of the intrinsic mechanical properties of the cellulose crystals. We demonstrate that CNC speeds up the assembly of fibroin in the hybrid dispersions, leading to the formation of more compact colloidal structures at the nanoscale than the sole SRSF. When the hybrid dispersions film, the presence of CNC favors the formation of crystalline structures (most notably α-helices) even at low fibroin concentration, and the films confer optimal axial strength to aged silk fibers, surpassing the performance of single-component (SRSF or CNC) dispersions at the same concentration of consolidant, and of pure crystalline SRSF. Overall, the hybrid formulations candidate as new sustainable tools for the preservation of historical textiles, employing renewable materials (cellulose and silk scraps) to restore artifacts.

1. Introduction

Silk artifacts, such as clothes, tapestries, banners and decorative items, constitute a valuable portion of mankind Cultural Heritage, spanning from ancient to modern times. These objects are typically made of degummed *Bombyx mori* cocoon's spun fibers [1], whose

* Correspondence to: Department of Chemistry and CSGI, University of Florence, via della Lastruccia 3, 50019, Sesto Fiorentino, Italy.
E-mail address: david.chelazzi@unifi.it (D. Chelazzi).

https://doi.org/10.1016/j.colsurfa.2021.127944
Received 21 October 2021; Received in revised form 17 November 2021; Accepted 18 November 2021
Available online 19 November 2021

composition and hierarchical structure account for their physical properties. Silk filaments (7–12 μm wide) are composed of fibrillar elements (~ 1 μm wide), which are in turn made of microfibrils (~ 10 nm wide). The proteins involved in this structural arrangement are mainly Heavy-Fibroin, Light-Fibroin, and the chaperonin-like P25 protein (6:6:1 ratio [2]), displaced along the fiber axis as amorphous and crystalline domains. As a result, the fibers exhibit optimal mechanical behavior, along with prize aesthetical features such as lightness, smoothness and luster, which overall have been making silk a desired fabric material since ages [3]. Unfortunately, silk is not immune to degradation that takes place during the natural aging of the artifacts. Diverse but concurring degradative pathways include hydrolysis and oxidation, induced by environmental factors (light, temperature, relative humidity and pollutants) and by the presence of acids, oxidizing compounds, metallic components and microorganisms [4–8]. The resulting chemical alterations, chain scissions, molecular and supramolecular rearrangements, change the fibers' secondary structure leading to fragility that hinders the conservation of aged silk artifacts as well as their safe handling, storage, exhibition and transfer [9–11].

In front of such challenges, the traditional restoration practice of historical textiles still relies on repairs and synthetic adhesives, but these methodologies have limitations and drawbacks that call for new consolidants to be developed. Repairs introduce new silk or paper elements to strengthen the textiles [12–14]; however, this approach does not provide effective reinforcement of the fibers, i.e. mechanically weak substrates will remain such, as no actual consolidation occurs at spatial scales down to the micron (or less). Synthetic polymers have good adhesion and mechanical properties, but compounds such as acrylates, vinyl acetates and epoxy resins can yellow over time, disfiguring the textiles, and lose acidic volatile organic compounds (VOCs, e.g. acetic acid); besides, the removability of these adhesives is hindered by their aging, creating yet another conservation challenge [15–17,56].

Hybrid materials [18] and biopolymers constitute a promising alternative to traditional approaches; in particular, the focus is on environmentally friendly materials that can be used to formulate consolidants [19] and composite systems [20] with desirable properties. Among them, fibroin and cellulose are optimal candidates: the first has, in principle, maximum physico-chemical compatibility with silk fibers, while the second, in particular in the form of cellulose nanofibrils (CNFs) and nanocrystals (CNC), exhibits ideal mechanical properties [21–23]. Not surprisingly, fibroin-silk and fibroin-nanocellulose composites are of great interest in the fields of biomaterials and materials engineering [24–30], but, to the best of our knowledge, their formulation and use in the restoration of aged silk textiles is still almost unexplored. Hao et al. have evaluated carboxymethyl chitosan (CMC)-silk fibroin composites for the reinforcement of aged silk, and found that CMC significantly enhances the mechanical improvement provided by fibroin on degraded silk fibers, likely thanks to interactions taking place between surface groups in chitosan and fibroin, leading to the formation of semi-interpenetrating structures [31].

Recently, we proposed a sustainable and inexpensive "green" method based on the use of waste silk scraps to restore fragile silk fibers [32]. Namely, self-regenerated silk fibroin (SRSF) films with controlled crystalline-amorphous content were obtained from fibroin dispersions (prepared from the scraps), by varying the concentration of the protein: high fibroin concentration (e.g. > 5% w/v) yielded SRSF films rich in β-sheets, and low concentration dispersions (0.3–0.2% w/v) produced films rich in random coils, with β-turns significantly present for intermediate values (1–2% w/v). When applied onto degraded textiles, highly amorphous films provided some recovering of the ductility of aged, fragile silk, likely due to the presence of domains with high fibroin chain mobility adhered to the silk fibers. Instead, highly crystalline (and thus brittle) films reduced the tensile strength and elongation length of the treated fibers, i.e. there appears to be an applicative limit to the concentration of fibroin consolidant in the dispersions.

Here, we propose to boost the consolidating effectiveness of SRSF amorphous films by blending fibroin with CNC, taking advantage of the ability of cellulose to form strong hydrogen bonds and electrostatic interactions with fibroin, inducing changes in the protein secondary structure (e.g. increase of β-sheets and decrease of random coils) and supramolecular arrangement. For instance, Xiong et al. showed that fibroin, extracted directly from *Bombyx mori* silkworm cocoons, can form structures with periodic arrangement of β-sheets and amorphous domains along segments of cellulose fibers, driven by modulation of crystalline phases, hydrogen bonding and hydrophobic interactions; such structures produced mechanically robust membranes [24]. We expected some fibroin structuration to take place also by blending SRSF, obtained with our approach, with CNC, and we hypothesized that the composite would thus exhibit higher effectiveness than pure amorphous SRSF in consolidating aged silk fibers, working at relatively low concentrations for each component (< 2% w/v) without the limitations of the sole highly crystalline SRSF. The hybrid SRSF-CNC formulation was physico-chemically characterized, investigating its self-assembly over time and its rheological behavior, and monitoring the formation of secondary structures in films cast from the composite as compared to the pure components. Then, the consolidating effect of the composite was assessed on silk fibers that had been aged through different degradative pathways, comparing it with pure SRSF or CNC dispersions, so as to evaluate the effectiveness and versatility of this novel silk restoration approach.

2. Experimental section

2.1. Materials

Ethanol (EtOH, CH_3CH_3OH, anhydrous, analytical grade, Carlo Erba), calcium chloride ($CaCl_2$, dehydrated powder, purity > 97.0%, Fluka), commercial white *taffetà* silk (Casa del tessuto, Florence), and cellulose nanocrystals (CNC, 0.7–0.8% of residual sulfur, Celluforce) were used for the preparation of the SRSF and hybrid SRSF-CNC dispersions. Ultrapure Milli-Q water (resistivity 18.2 MΩ.cm at 25 °C) was used where needed. Silver nitrate ($AgNO_3$, 0.1 M, Merck) was used for chloride assays. Commercial white *georgette* silk (Casa del tessuto, Firenze) was used for the preparation of pristine and aged silk mockups. Glycerol ($C_3H_8O_3$, purity > 99.5%, Sigma Aldrich) was used for the preparation of aqueous hygroscopic solutions for conditioning of the samples. Sulfuric acid (H_2SO_4, purity 96%, Carlo Erba) was used to induce the hydrolytic degradation of silk.

2.2. Silk mockups

Pristine, non-dyed *georgette* silk (labeled as "PS'') was used as reference silk textile and to prepare aged silk mockups. Alteration of the fibroin secondary structure and worsening of the mechanical properties of the silk fibers was carried out using three different types of treatment (thermal, acidic, UV-Vis light) on pristine silk [32], related to the main degradation processes that take place during natural aging and exposition in museums or collections. In all cases, silk samples of 20 × 30 cm^2 were treated.

Thermal aging was carried out by heating the silk samples in a convection oven (TCN 50 Plus, Argolab) at 130 °C for 4 h (samples labeled as "AS1″). Acidic aging was carried out by immersing the samples in an aqueous solution of sulfuric acid (pH=1) for 24 h; no rinsing was carried out, and then the fabric was let dry at room temperature for 3 days (samples labeled as "AS2″). Photo-oxidative aging (samples labeled as "AS3″) was carried out by placing the textile in a closed chamber irradiated with UV–Vis light (Neon Light Color 765 Basic daylight Beghelli lamp; 160 mW/lm, λ = 380–700 nm) for 30 days; the climatic conditions inside the chamber (T = 36 ± 2 °C and RH 40 ± 5%) were recorded through a digital thermohygrometer (Gauge). To ensure homogeneous irradiation of the samples, the chamber was also equipped with internal reflecting walls. The sample surface was exposed to 11000

Lux of homogeneous illumination, which accelerates the natural aging that affects textiles displayed in museums, where light levels of 50–100 lux are typically used.

2.3. SRSF, CNC and composite SRSF-CNC dispersions

The SRSF dispersions were obtained from scraps of taffeta silk, using a modified version of the protocol reported elsewhere [32]. The silk scraps underwent four washings in EtOH to remove industrial additives and impurities, and were dried at room temperature; then, the textile was ground and immersed in a solution of $CaCl_2$:H_2O:EtOH (molar ratio of 1:8:2), keeping a silk concentration of 0.1 g/mL. The bath was heated at 90 °C and stirred for 15 min. The solution was then dialyzed with a membrane cell (Dialysis tubing, high retention seamless cellulose tubing, MWCO 12400, 99.9% retention, Sigma Aldrich) for 48 h against 1 L water. Water was changed four times, and the dialysis bath was kept under magnetic stirring to facilitate the desalination process. The effective elimination of the salt was verified through $AgNO_3$ chloride assays. The dialyzed solution was centrifuged twice at 9000 rpm for ten minutes, and the supernatant separated. The final concentration of fibroin in the dispersion (2.70% w/v) was measured gravimetrically. Once the effective concentration of SRSF was calculated, the dispersion was analyzed or used for application on the silk mockups, either undiluted or diluted at desired concentrations (0.15–1.80% w/v). Aqueous CNC dispersions were prepared by magnetic stirring CNC powder into water for 5 h at room temperature. The dispersions were then sonicated for 5 min with 20% amplitude, using a Branson S-450 ultrasonifier equipped with micro-tip. Different concentrations (0.15–2.70% w/v) were used for analysis or application on the silk mockups. SRSF/CNC hybrid dispersions were prepared by mixing and magnetically stirring CNC and SRSF dispersions, keeping the same concentration of SRSF and CNC, in the 0.15%/0.15–1.35%/1.35% w/v range. The prepared dispersions are neutral (pH 6.5–7.0).

2.4. Zeta potential measurements

Zeta potential measurements were carried out using a 90Plus – Particle Size Analyzer (Brookhaven Instruments Corporation). The concentration of the analyzed dispersions was kept in the 0.30–0.60% range (w/v), to obtain as much as possible optically clear systems and avoid attenuation of the laser light. The PALS Zeta Potential Analyzer software (Brookhaven Instruments Corporation) was used to collect and analyze data. Four repeats were carried out for each sample.

2.5. Dynamic light scattering

Dynamic Light Scattering (DLS) measurements were performed on dispersions using a spectrometer (Brookhaven Instruments Corporation) equipped with a goniometer (BI200 SM), a correlator (BI 9000AT), a diode Nd YAG laser (Coherent Inova) operating at a wavelength of $\lambda =$ 532 nm as the light source, and a BI APD detector. Data were acquired and processed through Dynamic Light Scattering Software Ver. 5.78 (Brookhaven Instruments Corporation). The samples were measured at a temperature of 25 °C and the intensity of scattered radiation was detected at an angle of 90° with respect to the source. The CONTIN algorithm was used to analyze the autocorrelation function [33,34] and obtain intensity-weighted plots. DLS measurements were collected at two different times (right after the preparation of dispersions and 24 h later) to compare possible variations in the dimensional distribution of the aggregates dispersed in the various systems over time. Three repeats were carried out for each sample.

2.6. Particle size distribution

Particle size distribution measurements were carried out with a laser diffraction particle size analyzer Mastersizer 3000 equipped with a Hydro SV automatic wet dispersion unit (Malvern). Laser obscurations ranged from 1% to 8%. The dispersion unit agitator was set at 1800 rpm, and water was used as dispersant. Non-spherical particles were assumed, and the refractive index for the SRSF/CNC hybrid was set to 1.55. For the measurement, two light sources were used: a red laser He-Ne ($\lambda =$ 632.8 nm) and a blue led ($\lambda =$ 470 nm). The Malvern Mastersizer 3000 "general purpose" analysis model based on number density was used to evaluate data. As in DLS analyses, measurements were performed right after preparation of the dispersions and 24 h later. For each sample 20 repeats (acquisitions of 5 s) were performed, and an interval of 5 s was set between successive measurements.

2.7. Rheological measurements

Rheological measurements were performed on freshly prepared SRSF and hybrid dispersions with a DHR3 hybrid rheometer (TA Instruments) using a 40 mm smooth cone-plate geometry. Sample evaporation was found to be negligible over the duration of the experiments, as determined from repeated tests performed at different waiting times after sample loading. Flow curves spanning an interval of shear rates $10s^{-1} \leq \dot{\gamma} \leq 10^3 s^{-1}$ were used to determine the viscosity of the samples in the limit of high shear rates, η_∞. For each point along the curve, the shear rate was equilibrated for 20 s and data were acquired during a time interval of 10 s

2.8. Small angle X-ray scattering

Small Angle X-Ray Scattering curves were measured on freshly prepared SRSF and hybrid dispersions using a Xeuss 3.0HR (Xenocs) instrument equipped with a Genix^{3D} (Cu) X-Ray source ($\lambda = 1.34\mathring{A}^{-1}$) and a Dectris 1 M Eiger detector. Samples were contained in glass capillary tubes of thickness 1.5 mm. Data from each sample were acquired at Sample-Detector (S-D) distances of 450 mm and 1800 mm for 600 s and 7200 s, respectively. Intensities were normalized with respect to transmission and sample thickness, and azimuthally averaged using the software XSact. After data reduction, the contribution of the sample holder and solvent (water) was subtracted from the sample intensity. The wave vector range (Q-range) accessed in experiments was $5{\bullet}10^{-3}\mathring{A}^{-1} \leq Q \leq 6{\bullet}10^{-1}\mathring{A}^{-1}$. All data were modeled with the SasView Software.

2.9. Analysis of the fibroin secondary structures

SRSF and SRSF/CNC films were cast by dripping 10 μL of dispersion on glass slides sputtered with gold. The films were conditioned at RH= 40% for a week before analysis of the fibroin secondary structures by means of Fourier transform Infrared microscopy (μ-FTIR). The films were analyzed (without any pre-treatment) with a Cary 670 FTIR spectrophotometer coupled to a Cary 620 FTIR microscope (Agilent Technologies), using a 15x Cassegrain objective. Measurements were carried out in reflectance mode over the gold-sputtered reflective slides, while background spectra were collected on a gold-plated surface. This setup was preferred to Attenuated Total Reflectance (ATR), as the pressure applied during ATR measurements is known to induce structural changes in silk fibers, preventing the accurate characterization of the fibroin secondary structure via spectral deconvolution (peak fitting [8]). The experimental conditions were: spectral range of 3900–900 cm^{-1}, 512 scans for each acquisition, spectral resolution of 2 cm^{-1}, open windows. A 128 × 128 pixels Focal Plane Array (FPA) detector was used to carry out 2D μ-FTIR Imaging; the pixel size is 5.5 μm x 5.5 μm, and each pixel provides an independent spectrum from the sample's surface. Each analysis delivers spectra of a 700 × 700 μm^2 "tile". For each film, three "tiles" were acquired to check reproducibility. The deconvolution of the films' spectra was carried out using the multipeak fitting package of the Igor Pro software, version 7

(WaveMetrics, Inc), following a procedure previously reported [7]. The deconvoluted bands of amide I were assigned to the different protein secondary structures reported in the literature [35,36]: 1) (Tyr) side chains/aggregated strands, 1605–1615 cm^{-1}; 2) aggregate β-strand/intermolecular β-sheets (weak), 1616–1621 cm^{-1}; 3) intermolecular β-sheets (strong), 1622–1627 cm^{-1}; 4) intramolecular β-sheets (strong), 1628–1637 cm^{-1}; 5) random coils/extended chains, 1638–1646 cm^{-1}; 6) random coils, 1647–1655 cm^{-1}; 7) α-helices, 1656–1662 cm^{-1}; 8) β-turns, 1663–1670; 9) β-turns, 1671–1685; 10) β-turns, 1686–1696 cm^{-1}; 11) intermolecular β-sheets (weak), 1697–1703 cm^{-1}; 12) oxidation bands, 1704–1720 cm^{-1}. In the SRSF/CNC films, the weak OH bending band of adsorbed water in CNC (1639 cm^{-1}) partially overlaps with the random coil components of SRSF Amide I, which are thus slightly overestimated by spectral deconvolutions.

2.10. Application of the dispersions on aged silk

Silk mockups were treated with SRSF, CNC and SRSF/CNC dispersions at different concentrations. In all cases, the dispersions were applied right after their preparation. A set of treated silk samples was prepared for each type of aged silk (AS1–3) and PS. Each set was made of small silk strips (4.0 ×0.5 cm^2), with the long side parallel to the direction of the textile warp. The treatment consisted in dripping 15 μL of a specific dispersion over a silk strip, taking care of wetting the fibers homogeneously. The treated samples were let dry at room temperature and then conditioned in a container at 55% relative humidity (RH) for one week before analyses. The samples in each set were labeled according to the received aging and treatment, e.g.: AS1–1.80% SRSF, AS1–0.90%/0.90% SRSF/CNC etc.

For tensile tests on treated silk mockups, the PS and AS1–3 strips treated with the different SRSF and CNC dispersions were analyzed with a Discovery HR-3 rheometer from TA Instruments, equipped with an extension accessory for measuring the elongation at break (%) and the axial force at break (N). The gap length was set at 1 cm and the elongation speed at 94 μm/s. Untreated PS, AS1, AS2 and AS3 strips were kept as ''blanks''; the PS and AS1–3 mockups were also treated with 15 μL of water, so as to evaluate the effect caused by simply wetting the silk fibers. Seven repeats were carried out for every combination of aging/treatment, as well as for "blanks" and samples treated with water.

Color measurements on treated silk mockups (7 ×4 cm^2) were performed using a X-rite SP60 spectrophotometer equipped with an integrating sphere having a circular sampling spot (diameter = 1.5 cm). Colorimetric coordinates were obtained using standard illuminant D65 and a standard observer at 2°. The untreated *georgette* mockups (PS, AS1–3) were taken as standard. The color differences according to the CIELab (2000) equation were obtained using the formula below:

$$\Delta E_{00} = \sqrt{\left(\frac{\Delta L'}{K_L S_L}\right)^2 \left(\frac{\Delta C'}{K_C S_C}\right)^2 + \left(\frac{\Delta H'}{K_H S_H}\right)^2 + R_T \left(\frac{\Delta C'}{K_C S_C}\right)\left(\frac{\Delta H'}{K_H S_H}\right)} \quad (1)$$

where S_L, S_C, and S_H describe the visual perception of lightness (L), chroma (C) and hue (H). $\Delta H'$, $\Delta C'$ and $\Delta L'$ are the change in the same parameters. The rotation factor R_T corrects a deflection that occurs in the blue region. K_L, K_C and K_H correct the influence of the experimental observation conditions [37]. The colors are given in CIELab coordinates: L* corresponds to brightness (100 = white, 0 = black), a* to the red--green coordinate (+ = red, − = green), b* to the yellow-blue coordinate (+ = yellow, − = blue), and C* to vividness-dullness (100 = vivid, 0 = dull). Ten repeats were carried out for each sample.

3. Results and discussion

3.1. Self-assembly and rheological behavior of the dispersions

The SRSF, CNC and SRSF/CNC dispersions were analyzed by means of DLS, laser diffraction and rheological measurements, investigating concentration values < 2% for each component. The SRSF systems showed marked self-assembly right after their preparation. By looking at the DLS Intensity plots and particles size-distribution measurements, the fibroin dispersions (see Fig. 1a) exhibit polydisperse aggregates in the 10–100 nm range, as well as in the micron scale, even starting from the end of the dialysis and centrifugation steps. The size distribution at the nanoscale shifts to slightly higher values over 24 h (Fig. S1a), and macroscopic aggregates form (~mm), which are visible to the naked eye. Because these aggregates sediment, the micron to submillimiter size distribution (as measured by the laser diffraction particle size analyzer) narrows around ~ 2 μm (see Fig. S2a and S2b). Silk fibroin is known to self-assemble in water through hydrophobic and hydrophilic interactions that lead to chain folding and the formation of micelles in the 100–200 nm range; in turn, micelles can assemble into nanofibrils or larger globules, depending on fibroin concentration and on pH, e.g. charge screening around the protein isoelectric point (~ 4.2) favors larger aggregates [38]. However, in our case significant assembly seemed to take place at neutral pH, and aggregates up to the millimeter scale formed over a shorter time span (hours) than what is typically reported in the literature (days [39,40]).

When hybrid systems are analyzed (Fig. 1b-c and S1b-c), polydisperse aggregates in the 60–800 nm range are observed in SRSF/CNC 0.90%/0.90% (see Fig. 1c and S1c), along with micron- and millimeter-sized particles, either at 0 h or over 24 h from preparation. Also in this case, the bigger aggregates (mm-sized, visible to the naked eye) sediment, resulting in size distributions centered on ~ 2 μm (see Fig. S2c and S2d). SRSF/CNC 0.30%/0.30% exhibited narrower distributions in the 50–160 nm (0 h) or 190–240 nm (24 h), as shown in Fig. 1b and S1b. Overall, the aggregates' size increase in the hybrid formulations is consistent with the faster assembly process reported for composites of fibroin and cellulose nanofibers, as compared to pure protein dispersions [24]: fibroin is able to organize in domains along cellulose nanofibers, directed by modulated interfacial interactions with the heterogeneous surfaces of the amphiphilic cellulose fibrils [24]. Similar interactions might take place in our hybrid formulations; this is also suggested by the change in the Zeta potential from the negative charge of single components (ca. −7 mV for SRSF, and −32 mV for CNC [41]) to a substantially neutral value for SRSF/CNC (−0.07 ± 1.26 mV), which we explained by hypothesizing that polar groups in the composites' assemblies are less exposed, likely due to interactions between CNC carboxyls and SRSF amide groups. Some of the larger objects detected by DLS in the hybrid formulations might also, in principle, be partially due to large CNC particles: while the literature reports dimensions of 35–75 nm for cellulose nanocrystals [41], the DLS Intensity plots show both nanometric and larger aggregates (~500 nm) in the CNC dispersions either at 0 h or over 24 h from preparation (see Fig. 1d and S1d), along with micron- and millimeter-sized particles (Fig. S2e-f). However, because CNC dispersions are known to be stable, these objects were ascribed to impurities or clusters from the manufacturing process, rather than aggregates formed by the self-assembly of nanosized cellulose crystals.

Additional information on the nanoscale structure of the systems was obtained from SAXS measurements. Fig. 2 shows the scattering intensities $I(Q)$ measured for SRSF (Fig. 2a), CNC (Fig. 2b), and SRSF/CNC (Fig. 2c) samples right after their preparation.

The curves of CNC were modeled using a parallelepiped form factor [42] with dimensions $A < B < C$ (see SI for further details); the obtained fitting parameters are reported in Table S1. The parameters are closely comparable for different CNC samples, except for the scale parameter (K) that reflects different concentrations. The obtained value of the A axis (~ 3 nm), and the polydispersity index (PI_A = 0.4, necessary to describe the high-Q range of the spectra, indicating a relatively broad size distribution) are consistent with previous results on cellulose nanocrystals [19,43]. The value of B is considerably larger than A, indicating aggregation of the CNC particles, and the average aggregation

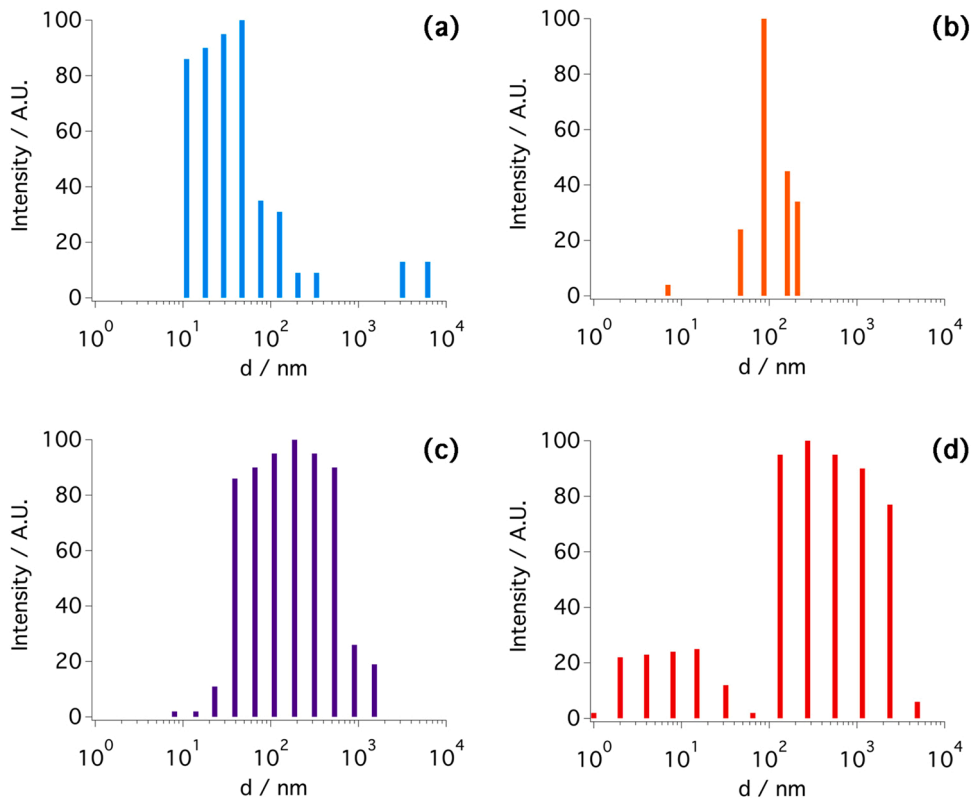

Fig. 1. DLS intensity-weighted plots measured for (a) SRSF (1.80% w/v), (b) SRSF/CNC (0.30%/0.30% w/v), (c) SRSF/CNC (0.90%/0.90% w/v) and (d) CNC (1.80% w/v) right after the preparation.

number $N_{agg} = \frac{B}{A} \approx 8$ is reasonable, considering previous data reported in the literature [43].

The SAXS intensity of the SRSF and SRSF/CNC samples was instead fitted using a mass fractal model, following the indication provided by the DLS measurements that assembly processes at the nanoscale occur in the fibroin-containing dispersions. In this case, the SAXS intensity was modeled as [44]:

$$I(Q) = K_1 P(Q) S(Q) + \text{bgd} \tag{2}$$

Where K_1 is a scale factor containing the contrast, bgd is a background factor, $P(Q)$ is the sphere form factor of the basic constituent of an aggregate:

$$P(Q) = \left\{ \frac{3[\sin(QR) - QR\cos(QR)]}{(QR)^3} \right\}^2 \tag{3}$$

being R the sphere radius. The structure factor $S(Q)$ is calculated as:

$$S(Q) = \frac{\Gamma(d_m - 1)\zeta^{d_m - 1} \sin[(d_m - 1)\tan^{-1}(q\zeta)]}{q\left[1 + (q\zeta)^2\right]^{(d_m - 1)/2}} \tag{4}$$

where d_m is the mass fractal dimension and ζ is the cutoff length, which provides an estimate of the aggregate size. The results of the fits are shown in Figs. 2b and 2c and the obtained parameters are reported in Table 1. The radius of the basic constituents is ~ 3.5 nm for SRSF 0.30%, decreasing to 2.9 nm for SRSF 0.90%, while slightly smaller values were found for the SRSF/CNC hybrids (2.7 nm for SRSF/CNC 0.30% and 2.4 nm for SRSF/CNC 0.90%); these sizes are characteristic of the hydrophobic domains of silk fibroin [45]. The values of d_m indicate, for both SRSF and SRSF/CNC, the presence of planar elongated aggregates [46], which we reasonably ascribed to the self-assembly of globular domains of the protein [45,47]. Interestingly, the cutoff length ζ, i.e. the characteristic aggregate size, is considerably higher for the pure SRSF samples (~67 nm) than the hybrids (12–13 nm). This, along with the larger fractal dimension exhibited by the SRSF/CNC samples, indicates the formation of more compact aggregates in the hybrid formulations, providing clear evidence for the effect of the addition of CNC on the SRSF assembly.

Fig. 3 reports the high-shear viscosity η_∞ extracted from flow curves measured at 0 h for SRSF, CNC and SRSF/CNC samples (an example of flow curve, for SRSF 0.90%, is shown in the figure inset).

For each sample, the value of η_∞ was extracted as the average value of the viscosity in the rate interval going from 10^2 to 5×10^2 s^{-1}. As expected, for all samples the viscosity increases with concentration, but the η_∞ increase of the hybrids is steeper than that of the pure components' dispersions. It is also clear that the viscosity of the hybrids is not the result of the sum of the individual viscosities of the correspondent SRSF and CNC dispersions. These results thus confirm the presence of significant interactions between SRSF and CNC in the hybrids, which affect the viscosity and lead to the changes in the microscopic structure, evidenced by the DLS, size distribution and SAXS measurements.

3.2. Fibroin secondary structures in pure and composite films

The effect of blending SRSF with CNC on the protein secondary structures of films obtained from the dispersions was investigated by casting fibroin and hybrid films right after the dispersions preparation, and analyzing them via μ-FTIR 2D Imaging coupled with spectral deconvolution. Results are shown in Fig. 4. In the visible light (VIS) maps, the films show iridescence, in some cases intense. Optical multilayer structures are known to produce structural coloration, coming from multiple layers of stacked domains with varying refractive indexes; in particular, fibroin can produce iridescent films where different colors stem from changes in film thickness and refractive index (which varies for different secondary structures [48]). The iridescent film layers are loosely alternated with fibrillar aggregates, whose size ranges from few

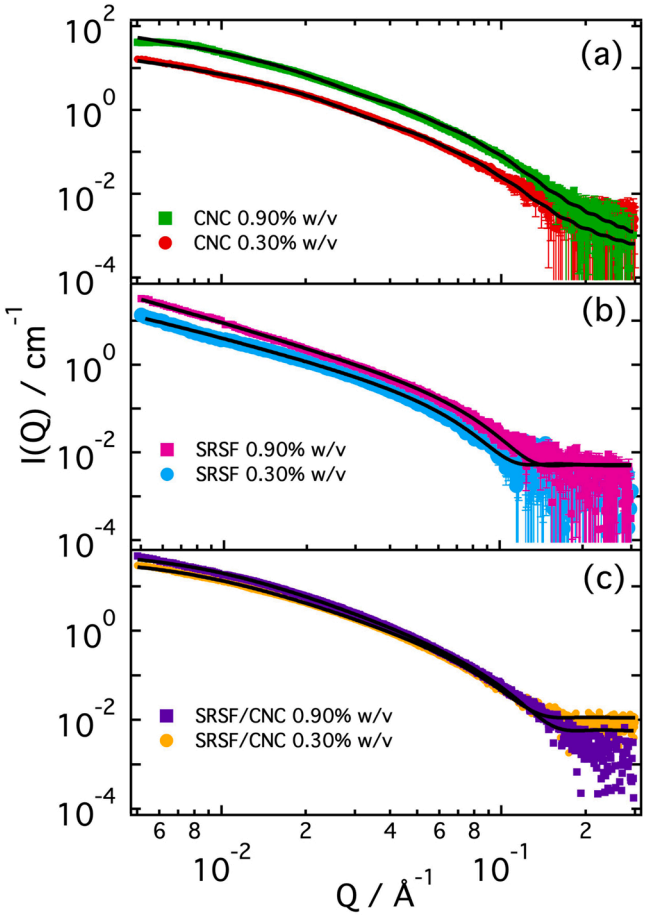

Fig. 2. SAXS spectra measured for (a) CNC (0.90%, 0.30% w/v, as indicated), (b) SRSF (0.90%, 0.30% w/v, as indicated), and (c) SRSF/CNC (0.90%/0.90%, 0.30%/0.30% w/v, as indicated) dispersions right after their preparation. Lines in (a) are fits of a parallelepiped form factor model, while lines in (b) and (c) are fits of a mass fractal model. The fitting parameters are reported in Table S1 and Table 1, respectively.

Table 1
Parameters obtained by fitting the mass fractal model of Eqs. (2–4) to the experimental data in Figs. 2b and 2c for samples SRSF 0.30%, SRSF 0.90%, SRSF/CNC 0.30% and SRSF/CNC 0.90%.

Fitting Parameter	SRSF 0.30%	SRSF 0.90%	SRSF/CNC 0.30%	SRSF/CNC 0.90%
K_1	0.0013 ± 0.0001	0.0014 ± 0.0001	0.0015 ± 0.0001	0.0012 ± 0.0002
R_0 (nm)	3.5 ± 0.1	2.9 ± 0.1	2.7 ± 0.1	2.4 ± 0.1
d_m	1.72 ± 0.01	1.95 ± 0.05	2.07 ± 0.01	2.24 ± 0.01
ζ (nm)	67 ± 5	67 ± 4	13.3 ± 0.2	11.7 ± 0.1
bgd	0.005 ± 0.0005	0.005 ± 0.001	0.011 ± 0.001	0.006 ± 0.001

microns to the millimeter; in general, such aggregates were found more frequently across the films' surfaces for hybrid formulations.

In the μ-FTIR 2D Imaging maps (700 ×700 μm^2), the pixel size is 5.5 × 5.5 μm^2, and each pixel provides an independent spectrum. This makes thousands of independent spectra collected on each film, allowing the identification of locations with representative and reproducible secondary structures, and the evaluation of average compositions in terms of the main structure types. For instance, simply mapping the films' absorbance at 1620 cm^{-1} (aggregate β-strand/intermolecular β-sheets, weak) qualitatively shows that the fibrillar aggregates are more

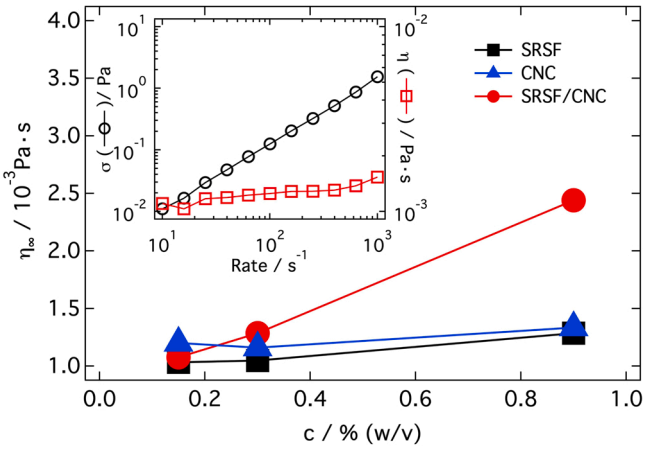

Fig. 3. High-shear viscosity η_∞ measured at 0 h for SRSF (full squares), CNC (full triangles) and SRSF/CNC (full circles) dispersions with concentration 0.15%, 0.30% and 0.90% w/v. Inset: Stress σ (open circles) and viscosity η (open squares) vs. rate for an example of flow curve (SRSF 0.90%). The value of η_∞ was extracted from the data region corresponding to rate values comprised between 10^2 and 5×10^2 s^{-1}. Error bars are smaller than markers.

structured than the rest of the film layers, while semi-quantitative information on the secondary structures was obtained via spectral deconvolution of the whole Amide I band. Fig. 4 reports the structural composition of films cast from SRSF (0.30%, 0.90% w/v) and SRSF/CNC (0.30%/0.30%, 0.90%/0.90% w/v); the weight of the main structure types (β-sheets, α-helices, β-turns, random coils, (Tyr) side chains/aggregated strands) was averaged from different locations on each film (indicated by numbers in the VIS and IR maps). The compositions of the pure SRSF films are consistent with those previously reported for films cast from SRSF dispersions at similar concentrations obtained with our synthetic approach, where increasing the protein concentration progressively leads to the increase of crystalline phases and β-turns at the expense of amorphous domains [32]. Interestingly, in all cases the addition of CNC causes a significant reduction of random coils and a marked increase in crystalline structures, most notably α-helices, for the same fibroin concentration. In the case of SRSF 0.30%, random coils decrease but do not disappear upon CNC addition, helices appear in significant amounts, while β-sheets and turns remain respectively around 15% and 30–35% of the total composition. Instead, for SRSF 0.90% introducing CNC completely depresses the presence of random domains, and strongly decreases β-turns; α-helices increase significantly, and β-sheets are also augmented. Even though it is not straightforward to fully explain the differences between the two hybrid systems, they exhibit similar trends, and it is evident that CNC causes ordering of the fibroin structures in the films. β-turns seem to represent an intermediate step in the transition from amorphous to crystalline films, an effect noticed also when fibroin concentration was increased in pure SRSF dispersions [32]. To the best of our knowledge, this is the first time a semi-quantitative evaluation is provided for the ordering of fibroin by nanocellulose, which has been previously qualitatively explained considering that the hydrophobic (hydrogen-rich) regions of cellulose nanofibers can act as hydrogen donors, maintaining fibroin β-sheets on their surface, while hydrophilic (oxygen-rich) regions facilitate structural changes in the protein by decreasing the interfacial hydrogen bonding between fibroin and cellulose [24]. Notably, in our case the addition of CNC produced crystalline structures that we could otherwise obtain only by markedly increasing the fibroin concentration in pure SRSF dispersions (i.e. > 5% w/v [32]). However, while casting highly concentrated fibroin dispersions on aged silk fibers produced brittle crystalline domains [32], we expected that the presence of CNC in the SRSF/CNC hybrid systems at lower protein concentrations (< 2%) would result in strong enhancement of the mechanical properties of

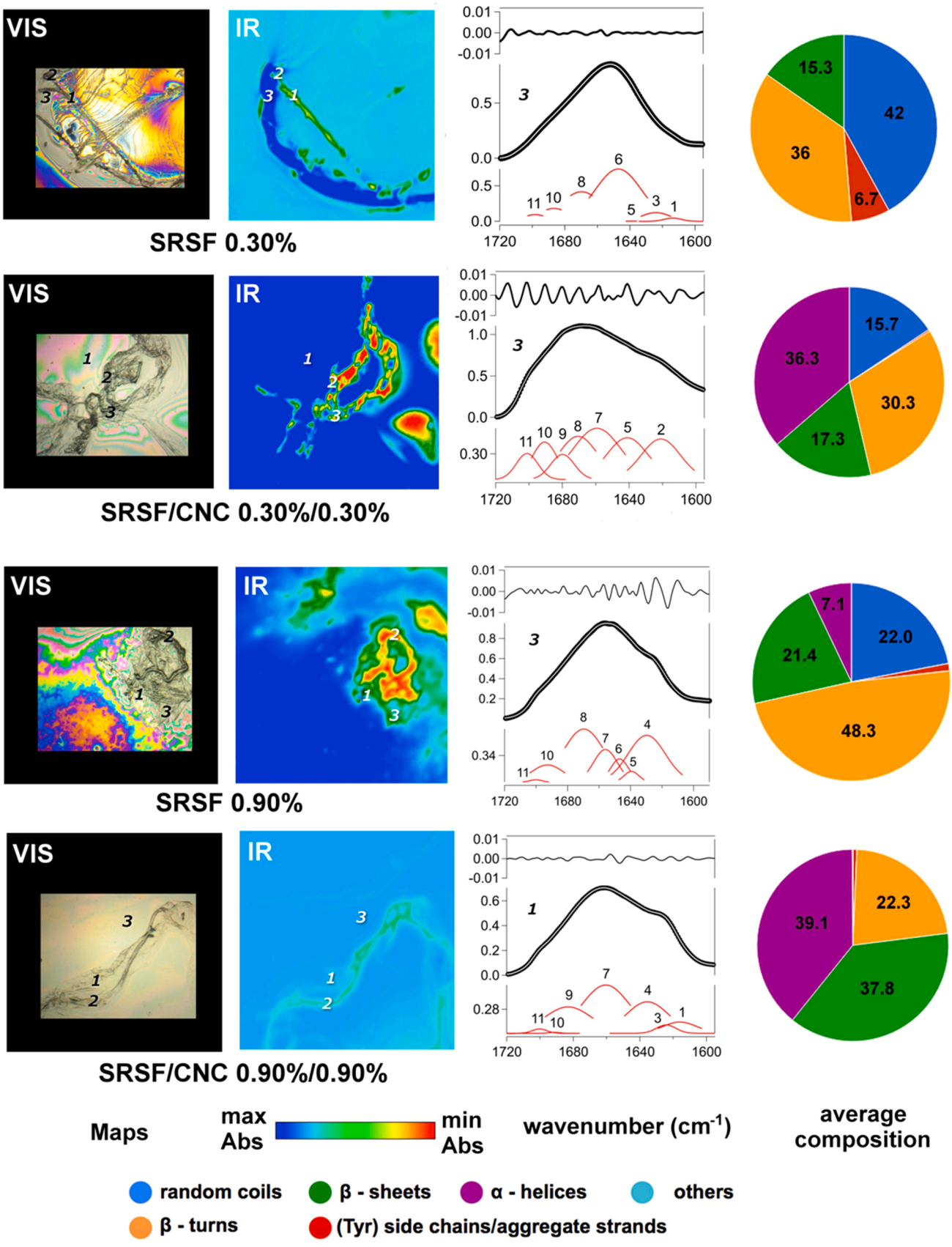

(caption on next page)

Fig. 4. Films cast from SRSF (0.30%, 0.90% w/v) and SRSF/CNC (0.30%/0.30%, 0.90%/0.90% w/v) dispersions on Au sputtered glass slides. The visible (VIS) and infrared (IR) maps show areas of 700 × 700 μm^2; in the false color IR maps, the intensity of the films' absorbance at 1620 cm^{-1} (aggregate β-strand/intermolecular β-sheets, weak) is imaged, using the chromatic scale: red > yellow > green > blue. Numbers on the maps indicate locations where the acquired IR spectra were deconvoluted to investigate the secondary structure of fibroin. For each film, a representative spectrum of one such location is shown in the 1720–1690 cm^{-1} region, along with the Amide I components, which are numbered in Section 2.9; the y-axis of the spectra reports the absorbance of the components (red bands), the experimental spectrum (black thick line), the fitting curve (thin white line inside the experimental curve), and the fitting residuals (black line on top of the spectra). The average secondary structure for each film (averaged on different locations, relative error is ca. 0.05) is reported in the pie charts, grouping the main structure types.

aged silk textiles. The improved mechanical behavior was hypothesized as a result of the organization of crystalline fibroin on cellulose fibers, and of the intrinsic mechanical properties of CNC.

3.3. Assessment of SRSF and SRSF/CNC dispersions for the consolidation of aged silk

The aged silk fibers were treated with SRSF, CNC and SRSF/CNC dispersions, and then their mechanical behavior was investigated. We previously showed that the fibroin dispersions penetrate the textile and adhere homogeneously to the fibers [32]. The axial force and elongation at break of silk fibers, before and after aging and treatment, is shown in Fig. 5 and S3. The effect of water and aqueous dispersions was evaluated separately. Namely, we compared the application of hybrid systems where the concentration of each component was either 0.90% or 1.35% (w/v), with that of single-component dispersions at twice the concentration (1.80% or 2.70%, respectively), so as to have overall the same mass of consolidant (SRSF, CNC, or SRSF plus CNC) added to the silk fibers in each case. Silk fibroin has high surface activity and, during film formation, is known to adsorb at the air/water interface decreasing the surface tension and producing high surface viscoelasticity; it has been shown, however, that the elastic modulus gain is restricted by the surface coverage limitation, i.e. the surface dilatational modulus decreases at high coverage owing to non-ideal arrangement of the fibroin molecules [49]. Taking into account this, and the previously reported formation of brittle SRSF domains at high protein concentrations [32], we kept the concentration of SRSF < 2% in the dispersions, and that of CNC < 3% so as to avoid gelation, which would prevent feasible application on the silk fibers.

Merely exposing silk (pristine or aged) to water causes a decrease of axial force at break and an increase of elongation at break (Fig. 5a and S3a), as water is known to interpose in the H-bonding networks of proteins and sugars, swelling the fibers and acting as a plasticizer [50–53]. Instead, some increase in axial force at break was observed on pristine silk when the hybrid dispersions are applied (Fig. 5a).

Most notably, the application of the hybrid systems produced significant improvements on the aged silk fibers, surpassing the performances of the single-component dispersions. On thermally aged samples (AS1 series), the SRSF/CNC 1.35%/1.35% hybrid proved the most effective, increasing significantly the axial force at break of the degraded textile almost back to that of pristine silk (see Fig. 5a-b) and maintaining the original elongation of the silk fibers (Figs. S3a-b). On samples exposed to acid (AS2 series), the hybrid formulations restored completely the axial force at break, and the 1.35%/1.35% system also recovered the original elongation (Fig. 5c and S3c). Finally, on photo-aged samples (AS3 series), where exposure to UV-Vis light causes embrittlement of the fibers by oxidation of amorphous chains and partial transformation of crystalline phases into less connected and disordered domains [7], the hybrid formulations restored the axial force at break back to that of pristine silk (or slightly higher), and the 0.90%/0.90% system also recovered completely the original elongation value (Fig. 5d and S3d). Differences in the behavior of samples exposed to different aging protocols are ascribable to the various effects of photo-, thermal and acid exposure on the silk fibers [7,32]. In all cases, the single-component dispersions provided some partial recovery of the axial force at break, but not as effectively as the hybrids. None of the

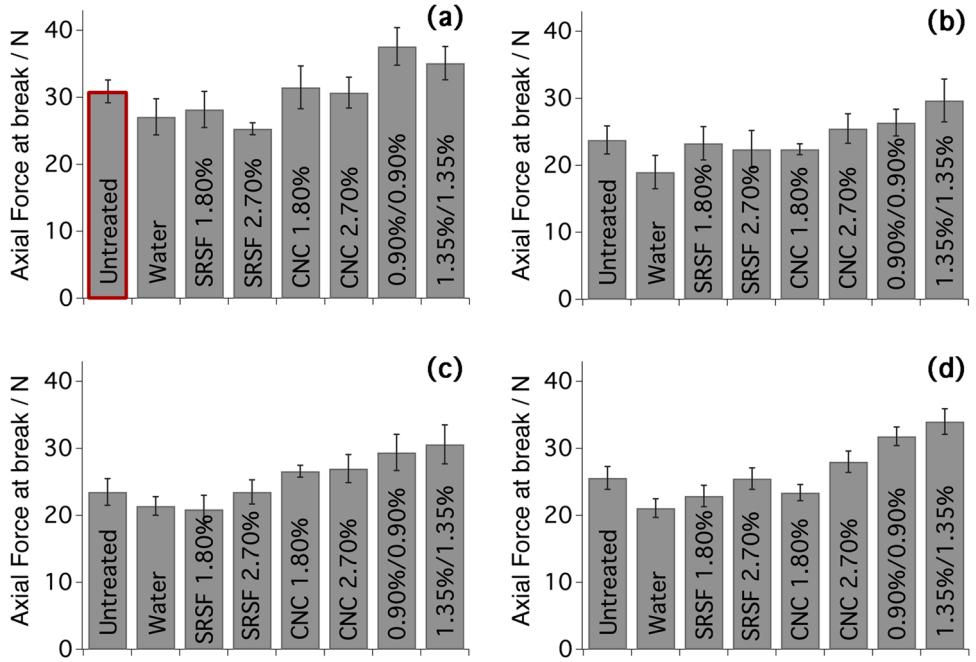

Fig. 5. Axial force at break of pristine (a) and aged silk mockups, namely AS1 (b), AS2 (c) and AS3 (d), treated with water, and with SRSF, CNC and hybrid SRSF/CNC formulations at different concentrations. Untreated silk (i.e. pristine or aged samples where formulations were not applied) is included as a reference in each graph. The hybrid formulations restored the axial force at break of the aged silk back to that of pristine silk (red boxed bar in panel a).

treatments altered significantly the color of the silk fibers, i.e. ΔE_{00} was always less than 2, which is deemed acceptable on Cultural Heritage objects [54].

The effectiveness of the hybrid SRSF/CNC formulations on all the different types of aged silk represents an added value: because natural aging of textiles in real conditions (museums, exhibitions, storages, archaeological sites) is likely to include exposure to light, temperature and acidic compounds, these hybrids stand out as promising and versatile tools to consolidate historical or archaeological silk objects.

4. CONCLUSIONS

We provided here, for the first time, the formulation, physicochemical characterization and application of hybrid SRSF/CNC colloidal dispersions tailored to the restoration of aged silk items. Our aim was to avoid too high fibroin concentrations that are known to produce brittle films (likely due to non-ideal arrangement of fibroin molecules at crowded interfaces), instead taking advantage of the protein structuration induced by cellulose nanocrystals to produce hybrid films with enhanced mechanical properties between fragile silk fibers, restoring the resistance of aged textiles.

The presence of CNC in the hybrid dispersions speeds up the assembly of fibroin, as demonstrated by DLS and laser diffraction measurements; SAXS analysis proved that CNC promotes the fast formation of aggregates that are more compact at the nanoscale as compared to pure SRSF assemblies. The occurrence of significant fibroin-cellulose interactions was also understood by the fact that viscosity increase with concentration in the hybrid dispersions is not directly additive, i.e. it is larger than the sum of the increases of single-component dispersions. When the hybrid dispersions film, the presence of CNC causes a significant reduction of random coils even in low-concentration fibroin formulations (which were known to otherwise produce mainly amorphous domains), and a marked increase in crystalline structures (most notably α-helices), evaluated semi-quantitatively via μ-FTIR 2D Imaging and spectral deconvolution.

Filming of the hybrid dispersions on aged silk textiles produced significant improvements of the fibers' mechanical behavior, restoring completely the axial force and maintaining optimal elongation at break; the hybrids provided the highest improvements, surpassing the performance of single-component dispersions at the same consolidant concentration, regardless the type of aging the silk fibers underwent before treatment. Such effectiveness and versatility make the SRSF/CNC dispersions optimal candidates for the restoration of aged silk artifacts, opening new perspectives in the preservation of our historical and artistic heritage. In addition, the use of renewable materials (cellulose and silk scraps) to formulate effective consolidants, follows the recommendations of the Green Deal [55], promoting the employment of sustainable materials and circular economy also in the art conservation sector.

Funding Sources

(Consorzio Interuniversitario per lo sviluppo dei Sistemi a Grande Interfase, Center for Colloid and Surface Science), Italy (CSGI) is gratefully acknowledged for financial support.

CRediT authorship contribution statement

All authors have given approval to the final version of the manuscript. C.C.: investigation, formal analysis, writing - original draft. D.C.: conceptualization, methodology, investigation, data analysis, supervision, writing - original manuscript, writing – Review & Editing, funding acquisition. G.P.: methodology, supervision, investigation and formal analysis. F.M.: investigation and formal analysis. R.G.: funding acquisition, supervision. M.L.: methodology, investigation, formal analysis, writing - original manuscript, writing – Review & Editing.

Competing interest

The authors declare no competing financial interest.

Declaration of Competing Interest

The authors declare that they have no known competing financial interests or personal relationships that could have appeared to influence the work reported in this paper.

Appendix A. Supporting information

Supplementary data associated with this article can be found in the online version at doi:10.1016/j.colsurfa.2021.127944.

References

[1] S.K. Vyas, S.R. Shukla, Comparative study of degumming of silk varieties by different techniques, J. Text. Inst. 107 (2016) 191–199, https://doi.org/10.1080/00405000.2015.1020670.
[2] S. Inoue, K. Tanaka, F. Arisaka, S. Kimura, K. Ohtomo, S. Mizuno, Silk Fibroin of Bombyx mori Is Secreted, Assembling a High Molecular Mass Elementary Unit Consisting of H-chain, L-chain, and P25, with a 6:6:1 Molar Ratio, J. Biol. Chem. 275 (2000) 40517–40528, https://doi.org/10.1074/jbc.M006897200.
[3] D. Kaplan, W.W. Adams, B. Farmer, C. Viney, Silk polymers, American Chemical Society,, Washington, DC, 1993, https://doi.org/10.1021/bk-1994-0544.
[4] N. Luxford, Silk durability and degradation, in: P.A. Annis (Ed.), Underst. Improv. Durab. Text., Woodhead Publishing, Oxford (UK), 2012, pp. 205–232, https://doi.org/10.1533/9780857097644.2.205.
[5] T. Asakura, T. Miller (Eds.), Biotechnology of Silk, Springer Netherlands, , Dordrecht, 2014, https://doi.org/10.1007/978-94-007-7119-2.
[6] F. Vilaplana, J. Nilsson, D.V.P. Sommer, S. Karlsson, Analytical markers for silk degradation: comparing historic silk and silk artificially aged in different environments, Anal. Bioanal. Chem. 407 (2015) 1433–1449, https://doi.org/10.1007/s00216-014-8361-z.
[7] D. Badillo-Sanchez, D. Chelazzi, R. Giorgi, A. Cincinelli, P. Baglioni, Characterization of the secondary structure of degummed Bombyx mori silk in modern and historical samples, Polym. Degrad. Stab. 157 (2018) 53–62, https://doi.org/10.1016/j.polymdegradstab.2018.09.022.
[8] D. Badillo-Sanchez, D. Chelazzi, R. Giorgi, A. Cincinelli, P. Baglioni, Understanding the structural degradation of South American historical silk: A Focal Plane Array (FPA) FTIR and multivariate analysis, Sci. Rep. 9 (2019) 17239, https://doi.org/10.1038/s41598-019-53763-5.
[9] P. Garside, P. Wyeth, Crystallinity and degradation of silk: correlations between analytical signatures and physical condition on ageing, Appl. Phys. A. 89 (2007) 871–876, https://doi.org/10.1007/s00339-007-4218-z.
[10] P. Garside, S. Lahlil, P. Wyeth, Characterization of historic silk by polarized attenuated total reflectance fourier transform infrared spectroscopy for informed conservation, Appl. Spectrosc. 59 (2005) 1242–1247, https://doi.org/10.1366/000370205774430855.
[11] Y. Gong, L. Li, D. Gong, H. Yin, J. Zhang, Biomolecular evidence of silk from 8,500 years ago, PLoS One 11 (2016), e0168042, https://doi.org/10.1371/journal.pone.0168042.
[12] H.E. Ahmed, Y.E. Ziddan, A new approach for conservation treatment of a silk textile in Islamic Art Museum, Cairo, J. Cult. Herit. 12 (2011) 412–419, https://doi.org/10.1016/j.culher.2011.02.004.
[13] Y. Nishio, Maintenance of Asian paintings II: minor treatment of scroll paintings, B. Pap. Gr. Annu. 20 (2002) 15–26.
[14] J.B. Perjés, K.E. Nagy, M.K. Bendefy, P.M. Kovács, E. Sipos, Conserving textiles: studies in honour of Ágnes Timár-Balázsy, ICCROM, Rome (IT), 2004.
[15] O. Chiantore, M. Lazzari, Photo-oxidative stability of paraloid acrylic protective polymers, Polymer 42 (2001) 17–27, https://doi.org/10.1016/S0032-3861(00)00327-X.
[16] M. Lazzari, O. Chiantore, Thermal-ageing of paraloid acrylic protective polymers, Polymer 41 (2000) 6447–6455, https://doi.org/10.1016/S0032-3861(99)00877-0.
[17] S.-Q. Wu, M.-Y. Li, B.-S. Fang, H. Tong, Reinforcement of vulnerable historic silk fabrics with bacterial cellulose film and its light aging behavior, Carbohydr. Polym. 88 (2012) 496–501, https://doi.org/10.1016/j.carbpol.2011.12.033.
[18] K. Kolman, O. Nechyporchuk, M. Persson, K. Holmberg, R. Bordes, Preparation of silica/polyelectrolyte complexes for textile strengthening applied to painting canvas restoration, Colloids Surf. A Physicochem. Eng. Asp. 532 (2017) 420–427, https://doi.org/10.1016/j.colsurfa.2017.04.051.
[19] Q. Xu, G. Poggi, C. Resta, M. Baglioni, P. Baglioni, Grafted nanocellulose and alkaline nanoparticles for the strengthening and deacidification of cellulosic artworks, J. Colloid Interface Sci. 576 (2020) 147–157, https://doi.org/10.1016/j.jcis.2020.05.018.
[20] N. Palladino, M. Hacke, G. Poggi, O. Nechyporchuk, K. Kolman, Q. Xu, M. Persson, R. Giorgi, K. Holmberg, P. Baglioni, R. Bordes, Nanomaterials for combined stabilisation and deacidification of cellulosic materials—the case of iron-tannate

dyed cotton, Nanomaterials 10 (2020) 900, https://doi.org/10.3390/nano10050900.
[21] K. Kolman, O. Nechyporchuk, M. Persson, K. Holmberg, R. Bordes, Combined nanocellulose/nanosilica approach for multiscale consolidation of painting canvases, ACS Appl. Nano Mater. (2018), https://doi.org/10.1021/acsanm.8b00262.
[22] O. Nechyporchuk, K. Kolman, A. Bridarolli, M. Odlyha, L. Bozec, M. Oriola, G. Campo-Francés, M. Persson, K. Holmberg, R. Bordes, On the potential of using nanocellulose for consolidation of painting canvases, Carbohydr. Polym. 194 (2018) 161–169, https://doi.org/10.1016/j.carbpol.2018.04.020.
[23] O. Nechyporchuk, J. Yu, V.A. Nierstrasz, R. Bordes, Cellulose nanofibril-based coatings of woven cotton fabrics for improved inkjet printing with a potential in E-textile manufacturing, ACS Sustain. Chem. Eng. 5 (2017) 4793–4801, https://doi.org/10.1021/acssuschemeng.7b00200.
[24] R. Xiong, H.S. Kim, S. Zhang, S. Kim, V.F. Korolovych, R. Ma, Y.G. Yingling, C. Lu, V.V. Tsukruk, Template-guided assembly of silk fibroin on cellulose nanofibers for robust nanostructures with ultrafast water transport, ACS Nano 11 (2017) 12008–12019, https://doi.org/10.1021/acsnano.7b04235.
[25] L. Wang, R. Lu, J. Hou, X. Nan, Y. Xia, Y. Guo, K. Meng, C. Xu, X. Wang, B. Zhao, Application of injectable silk fibroin/graphene oxide hydrogel combined with bone marrow mesenchymal stem cells in bone tissue engineering, Colloids Surf. A Physicochem. Eng. Asp. 604 (2020), 125318, https://doi.org/10.1016/j.colsurfa.2020.125318.
[26] L. Wang, G.-L. Ning, M. Senna, Microstructure and gelation behavior of hydroxyapatite-based nanocomposite sol containing chemically modified silk fibroin, Colloids Surf. A Physicochem. Eng. Asp. 254 (2005) 159–164, https://doi.org/10.1016/j.colsurfa.2004.12.003.
[27] L. Zhou, Q. Wang, J. Wen, X. Chen, Z. Shao, Preparation and characterization of transparent silk fibroin/cellulose blend films, Polym. (Guildf.) 54 (2013) 5035–5042, https://doi.org/10.1016/j.polymer.2013.07.002.
[28] Y. Feng, X. Li, M. Li, D. Ye, Q. Zhang, R. You, W. Xu, Facile preparation of biocompatible silk fibroin/cellulose nanocomposite films with high mechanical performance, ACS Sustain. Chem. Eng. 5 (2017) 6227–6236, https://doi.org/10.1021/acssuschemeng.7b01161.
[29] D. Yan, L. Qiu, K.J. Shea, Z. Meng, M. Xue, Dyeing and functionalization of wearable silk fibroin/cellulose composite by nanocolloidal array, ACS Appl. Mater. Interfaces 11 (2019) 39163–39170, https://doi.org/10.1021/acsami.9b11576.
[30] P. Wongpanit, N. Sanchavanakit, P. Pavasant, T. Bunaprasert, Y. Tabata, R. Rujiravanit, Preparation and characterization of chitin whisker-reinforced silk fibroin nanocomposite sponges, Eur. Polym. J. 43 (2007) 4123–4135, https://doi.org/10.1016/j.eurpolymj.2007.07.004.
[31] X. Hao, X. Wang, W. Yang, J. Ran, F. Ni, T. Tong, W. Dai, L. Zheng, X. Shen, H. Tong, Comparisons of the restoring and reinforcement effects of carboxymethyl chitosan-silk fibroin (Bombyx mori/Antheraea Yamamai/Tussah) on aged historic silk, Int. J. Biol. Macromol. 124 (2019) 71–79, https://doi.org/10.1016/j.ijbiomac.2018.11.203.
[32] D. Chelazzi, D. Badillo-Sanchez, R. Giorgi, A. Cincinelli, P. Baglioni, Self-regenerated silk fibroin with controlled crystallinity for the reinforcement of silk, J. Colloid Interface Sci. 576 (2020) 230–240, https://doi.org/10.1016/j.jcis.2020.04.114.
[33] S.W. Provencher, A constrained regularization method for inverting data represented by linear algebraic or integral equations, Comput. Phys. Commun. 27 (1982) 213–227, https://doi.org/10.1016/0010-4655(82)90173-4.
[34] S.W. Provencher, CONTIN: a general purpose constrained regularization program for inverting noisy linear algebraic and integral equations, Comput. Phys. Commun. 27 (1982) 229–242, https://doi.org/10.1016/0010-4655(82)90174-6.
[35] X. Hu, D. Kaplan, P. Cebe, Determining beta-sheet crystallinity in fibrous proteins by thermal analysis and infrared spectroscopy, Macromolecules 39 (2006) 6161–6170, https://doi.org/10.1021/ma0610109.
[36] J. KONG, S. YU, Fourier transform infrared spectroscopic analysis of protein secondary structures, Acta Biochim. Biophys. Sin. (Shanghai). 39 (2007) 549–559, https://doi.org/10.1111/j.1745-7270.2007.00320.x.
[37] M.R. Luo, G. Cui, B. Rigg, The development of the CIE 2000 colour-difference formula: CIEDE2000, Color Res. Appl. 26 (2001) 340–350, https://doi.org/10.1002/col.1049.
[38] Q. Lu, H. Zhu, C. Zhang, F. Zhang, B. Zhang, D.L. Kaplan, Silk self-assembly mechanisms and control from thermodynamics to kinetics, Biomacromolecules 13 (2012) 826–832, https://doi.org/10.1021/bm201731e.
[39] S. Ling, C. Li, J. Adamcik, Z. Shao, X. Chen, R. Mezzenga, Modulating materials by orthogonally oriented β-strands: composites of amyloid and silk fibroin fibrils, Adv. Mater. 26 (2014) 4569–4574, https://doi.org/10.1002/adma.201400730.
[40] S. Ling, C. Li, J. Adamcik, S. Wang, Z. Shao, X. Chen, R. Mezzenga, Directed growth of silk nanofibrils on graphene and their hybrid nanocomposites, ACS Macro Lett. 3 (2014) 146–152, https://doi.org/10.1021/mz400639y.
[41] S. Shafiei-Sabet, W.Y. Hamad, S.G. Hatzikiriakos, Rheology of nanocrystalline cellulose aqueous suspensions, Langmuir 28 (2012) 17124–17133, https://doi.org/10.1021/la303380v.
[42] R. Nayuk, K. Huber, Formfactors of hollow and massive rectangular parallelepipeds at variable degree of anisometry, Z. Für Phys. Chem. 226 (2012) 837–854, https://doi.org/10.1524/zpch.2012.0257.
[43] M. Uhlig, A. Fall, S. Wellert, M. Lehmann, S. Prévost, L. Wågberg, R. von Klitzing, G. Nyström, Two-dimensional aggregation and semidilute ordering in cellulose nanocrystals, Langmuir 32 (2016) 442–450, https://doi.org/10.1021/acs.langmuir.5b04008.
[44] D.F.R. Mildner, P.L. Hall, Small-angle scattering from porous solids with fractal geometry, J. Phys. D. Appl. Phys. 19 (1986) 1535–1545, https://doi.org/10.1088/0022-3727/19/8/021.
[45] H. Shulha, C.W. Po Foo, D.L. Kaplan, V.V. Tsukruk, Unfolding the multi-length scale domain structure of silk fibroin protein, Polym. (Guildf.) 47 (2006) 5821–5830, https://doi.org/10.1016/j.polymer.2006.06.002.
[46] F. Soto-Bustamante, N.E. Valádez-Pérez, R. Castañeda-Priego, M. Laurati, Potential-invariant network structures in Asakura–Oosawa mixtures with very short attraction range, J. Chem. Phys. 155 (2021), 034903, https://doi.org/10.1063/5.0052273.
[47] J. Zhong, M. Ma, W. Li, J. Zhou, Z. Yan, D. He, Self-assembly of regenerated silk fibroin from random coil nanostructures to antiparallel β-sheet nanostructures, Biopolymers 101 (2014) 1181–1192, https://doi.org/10.1002/bip.22532.
[48] Q. Li, N. Qi, Y. Peng, Y. Zhang, L. Shi, X. Zhang, Y. Lai, K. Wei, I.S. Kim, K.-Q. Zhang, Sub-micron silk fibroin film with high humidity sensibility through color changing, RSC Adv. 7 (2017) 17889–17897, https://doi.org/10.1039/C6RA28460D.
[49] X. Qiao, R. Miller, E. Schneck, K. Sun, Foaming properties and the dynamics of adsorption and surface rheology of silk fibroin at the air/water interface, Colloids Surf. A Physicochem. Eng. Asp. 591 (2020), 124553, https://doi.org/10.1016/j.colsurfa.2020.124553.
[50] H. KIM, D. SEO, Effect of water absorption fatigue on mechanical properties of sisal textile-reinforced composites, Int. J. Fatigue 28 (2006) 1307–1314, https://doi.org/10.1016/j.ijfatigue.2006.02.018.
[51] X. Hu, D. Kaplan, P. Cebe, Effect of water on the thermal properties of silk fibroin, Thermochim. Acta 461 (2007) 137–144, https://doi.org/10.1016/j.tca.2006.12.011.
[52] G.R. Plaza, P. Corsini, J. Pérez-Rigueiro, E. Marsano, G.V. Guinea, M. Elices, Effect of water onBombyx mori regenerated silk fibers and its application in modifying their mechanical properties, J. Appl. Polym. Sci. 109 (2008) 1793–1801, https://doi.org/10.1002/app.28288.
[53] K. Yazawa, K. Ishida, H. Masunaga, T. Hikima, K. Numata, Influence of water content on the β-sheet formation, thermal stability, water removal, and mechanical properties of silk materials, Biomacromolecules 17 (2016) 1057–1066, https://doi.org/10.1021/acs.biomac.5b01685.
[54] O. García, K. Malaga, Definition of the procedure to determine the suitability and durability of an anti-graffiti product for application on cultural heritage porous materials, J. Cult. Herit. 13 (2012) 77–82, https://doi.org/10.1016/j.culher.2011.07.004.
[55] J.B. Skjærseth, Towards a European Green Deal: the evolution of EU climate and energy policy mixes, Int. Environ. Agreem. Polit. Law Econ. 21 (2021) 25–41, https://doi.org/10.1007/s10784-021-09529-4.
[56] D. Chelazzi, A. Chevalier, G. Pizzorusso, R. Giorgi, M. Menu, P. Baglioni, Characterization and degradation of poly(vinyl acetate)-based adhesives for canvas paintings, Polymer Degradation and Stability 107 (2014) 314–320, https://doi.org/10.1016/j.polymdegradstab.2013.12.028.